

Article

Microstructure and Magnetic Properties of Grain Refined $\text{Pr}_2\text{Co}_{14}\text{B}$ Melt-Spun Ribbons

I. C. Nlebedim^{1,*}, M. Huang¹, K. Sun^{1,2}, L. Zhou^{1,2}, R. W. McCallum^{1,2} and M. J. Kramer^{1,2}

¹ Critical Materials Institute, Ames Laboratory, U.S. DOE, Ames, IA 50014, USA; mianlianghuang@gmail.com (M.H.); seraphsunkw@hotmail.com (K.S.); linzhou@ameslab.gov (L.Z.); rwmccallum@msn.com (R.W.M.); mjkrmer@ameslab.gov (M.J.K.)

² Division of Materials Science and Engineering, Ames Laboratory, U.S. DOE, Ames, IA 50014, USA

* Correspondence: nlebedim@iastate.edu; Tel.: +1-(515)-294-8916

Received: 29 November 2018; Accepted: 3 January 2019; Published: 22 January 2019



Abstract: The correlation between the grain refining effect of TiC on the microstructure of $\text{Pr}_2\text{Co}_{14}\text{B}$ melt-spun ribbons and the magnetic properties is presented in this study. TiC enabled greater control of microstructure both in the as-spun and heat treated $\text{Pr}_2\text{Co}_{14}\text{B}$, compared with the material without TiC. As a result, coercivity of the sample with TiC was nearly twice that of the sample without TiC. In addition to $\text{Pr}_2\text{Co}_{14}\text{B}$, two other phases were found in the sample with TiC: one rich in Co and the other having a composition near PrCo_2 . TiC was found near the grain boundaries and at triple junctions. Also no Ti or C was found in the matrix phase indicating extreme low solubility of the elements when both are present with $\text{Pr}_2\text{Co}_{14}\text{B}$. As expected, both the samples with and without TiC have similar anisotropy field but the presence of room temperature non-ferromagnetic phases (TiC and PrCo_2), caused a small decrease in magnetization of the sample with TiC although the romance of the isotropic materials were comparable.

Keywords: microstructure; permanent magnets; $\text{Pr}_2\text{Co}_{14}\text{B}$; TiC; melt spun ribbons; transmission electron microscopy (TEM); refractory carbides

1. Introduction

The high intrinsic coercivity and outstanding maximum energy product of sintered $\text{Nd}_2\text{Fe}_{14}\text{B}$ magnets [1,2] make them excellent candidates for many applications in electric motors, medical devices, generators, speakers, sensors, transducers and consumer electronics [3,4]. However, due to the relatively low Curie temperature (585 K), $\text{Nd}_2\text{Fe}_{14}\text{B}$ magnets lack sufficient thermal stability above 380–450 K [5]. Studies have been performed to enhance temperature dependence of the magnetic properties of the $\text{Nd}_2\text{Fe}_{14}\text{B}$ magnets by both composition and microstructural modifications [1,2,6–8]. Dy has been added to enhance coercivity and high temperature performance of $\text{Nd}_2\text{Fe}_{14}\text{B}$ [4,9–12] but maximum operating temperature of commercial grade materials are still limited to ≤ 500 K [13,14]. Moreover, the forecasted long term criticality and high cost of Dy could become a major obstacle to the production of Dy-enhanced $\text{Nd}_2\text{Fe}_{14}\text{B}$ magnets [3]. Therefore, it is of interest to advance research in developing alternative magnet materials with high Curie temperature, high coercivity and reasonable energy product. Although such alternative permanent magnets may lack in some magnetic performance, for example, energy product, compared to $\text{Nd}_2\text{Fe}_{14}\text{B}$, they can serve as substitutes where applicable. Even if the substitutes contain other materials deemed critical, e.g. cobalt, they will enable source diversification which is a good strategy for mitigating materials supplies problems. Such substitution approach is currently applied towards mitigating supply risks for cobalt in batteries [15,16].

$\text{Nd}_2\text{Co}_{14}\text{B}$ and $\text{Nd}_2\text{Fe}_{14}\text{B}$ can form a continuous solid solution in $\text{Nd}_2\text{Co}_x\text{Fe}_{14-x}\text{B}$ [17]. It is reported that Curie temperature increases monotonically with Co content in $\text{Nd}_2\text{Co}_x\text{Fe}_{14-x}\text{B}$ [2,18] and

reaches 995 K at $x = 14$ [17] (i.e., when all Fe are replaced by Co). However the saturation magnetization and anisotropy field of $\text{Nd}_2\text{Co}_{14}\text{B}$ are much lower than those of $\text{Nd}_2\text{Fe}_{14}\text{B}$ [19]. By substituting Nd with Pr to form $\text{Pr}_2\text{Co}_{14}\text{B}$, an anisotropy field (~ 75 T at 4.2 K) can be obtained. This is more than twice that of $\text{Nd}_2\text{Co}_{14}\text{B}$ (30 T at 4.2 K) obtained by extrapolation of magnetization data in aligned samples [20]. At room temperature, an anisotropy field higher than 12.6 T was reported for $\text{Pr}_2\text{Co}_{14}\text{B}$ by Shimao et al. [21]. This high anisotropy field indicates the possibility of developing $\text{Pr}_2\text{Co}_{14}\text{B}$ -based magnets with high coercivity. For example, coercivity of 15–25 kOe were reported by Fuerst et al. [22] and Christodoulou [19] in melt-spun ribbons. In the Nd-Fe-B system, it is known that addition of TiC refines grain sizes and leads to enhanced coercivity [23,24]. Such effect of refractory carbides on the microstructure of $\text{Pr}_2\text{Co}_{14}\text{B}$ and the corresponding magnetic properties, is not well known. As a result, this study evaluates the relationship between microstructure and magnetic properties of $\text{Pr}_2\text{Co}_{14}\text{B}$ due to grain refinement with TiC.

2. Materials and Method

Ingots of $\text{Pr}_2\text{Co}_{14}\text{B}$, with and without TiC, were made by arc melting of the constituent elements in Ar atmosphere. All samples were synthesized in the laboratory. Ribbons, with average thickness of ~ 30 μm , were made by melting the ingots contained in quartz crucibles under high purity He gas and ejecting the melt onto a single Cu wheel at a wheel speed of 30 m/s. The $\text{Pr}_2\text{Co}_{14}\text{B}$ samples without TiC are hereafter referred to as PrCoB and the samples with 3 wt.% TiC are hereafter referred to as PrCoB-TiC. Some of the as-spun PrCoB and PrCoB-TiC were wrapped with Ta foil, sealed in a quartz tube filled with high purity Ar and annealed at 1020 K for 15 min. The samples were quenched in water to ambient conditions. Powders derived from grinding the ribbons were used for crystal structure analysis using $\text{Co } K_\alpha$ radiation for X-ray diffractometry (XRD). The phases were determined by comparing the XRD patterns with powder diffraction files (PDF cards). Microstructural characterization was performed on a probe aberration corrected FEI Titan Themis scanning transmission electron microscope (TEM) with Super-X energy dispersive X-ray (EDS) detector. The TEM samples were prepared by mechanical wedge polishing followed by argon ion milling with liquid N_2 cold stage.

Simultaneous thermal analyses (STA) including thermogravimetry analysis (TGA) and differential scanning calorimetry (DSC) were performed at a heating rate of 20 K/min to determine the Curie temperature and spin reorientation temperatures of the alloys. A pair of permanent magnets attached to the STA system creates a magnetic field gradient on the sample. Changes in the permeability reflecting changes in magnetic anisotropy at the spin reorientation temperature and magnetic order at the Curie temperature, result in an apparent mass changes [25]. Magnetization was measured using a vibrating sample magnetometer up to a maximum applied magnetic field of 90 kOe. In order to measure the anisotropy field, ingots were sealed in quartz tube, annealed at 1270 K for 7 days and slowly cooled in furnace to ambient conditions. The annealed ingots were pulverized by ball milling and sieved to grain sizes < 20 μm . The powders were aligned in a 1.5 T magnetic field and cured in an epoxy resin with the magnetic field applied. Magnetization was measured with the applied field both parallel and perpendicular to the alignment direction in order to determine the anisotropy field. The anisotropy field H_A was derived from the intersection points of the extrapolated magnetization plots in parallel and perpendicular directions.

3. Results and Discussion

Figure 1a,b show the TGA and DSC plots of the as-spun PrCoB-TiC and PrCoB ribbons, respectively. In Figure 1a, the absence of a spin-reorientation peak in the TGA curve indicates that the $\text{Pr}_2\text{Co}_{14}\text{B}$ phase is mostly in the amorphous state in the as-spun PrCoB-TiC. In Figure 1b, the peak corresponding to the spin-reorientation temperature is seen for the as-spun PrCoB at 670 K, indicating the formation of mostly crystalline materials. The crystallization activity of the PrCoB-TiC at ~ 930 K (Figure 1a) is less pronounced compared to that of PrCoB at ~ 920 K in Figure 1b. This further confirms

that the sample PrCoB-TiC has more amorphous fraction compared PrCoB-TiC. The ~10 K difference in the crystallization temperatures can be attributed to the grain refinement effect of TiC leading to delayed crystallization.

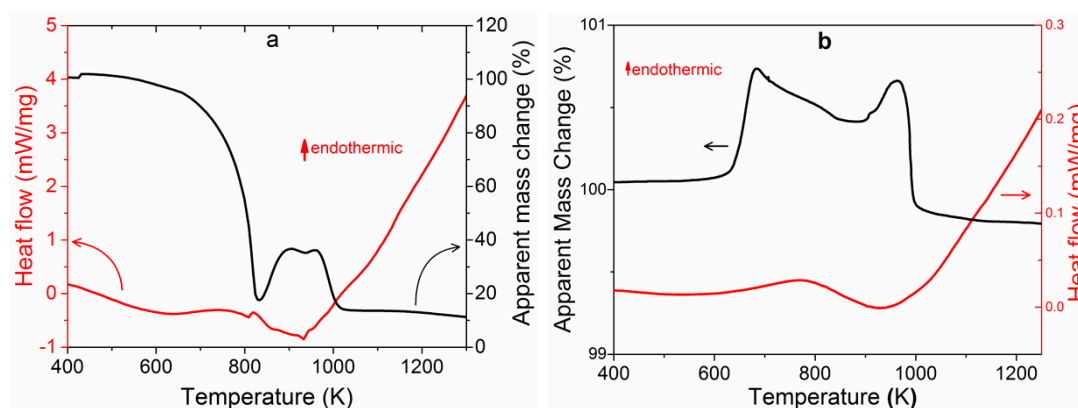


Figure 1. TGA (black plots) and DSC (red plots) of $\text{Pr}_2\text{Co}_{14}\text{B}$ as-spun ribbons with TiC (a) and without TiC (b), the analysis was performed in a gradient magnetic field.

From the TGA plots, Curie temperatures of 1038 K and 1013 K were obtained for the as-spun PrCoB-TiC and PrCoB samples, respectively. The obtained Curie temperature is higher than previously reported for the Pr-Co-B system and may be related to compositionally non-equilibrium state in the as-spun ribbons. This was verified by performing TGA measurement in magnetic field on as-spun ribbons of PrCoB annealed for seven days at 1270 K. The results (Figure 2) shows a Curie temperature of 989 K which is between the values reported by Pedziwiatr (986 K) [26] and Shimao (998 K) [21]. It also shows a spin-reorientation at 681 K.

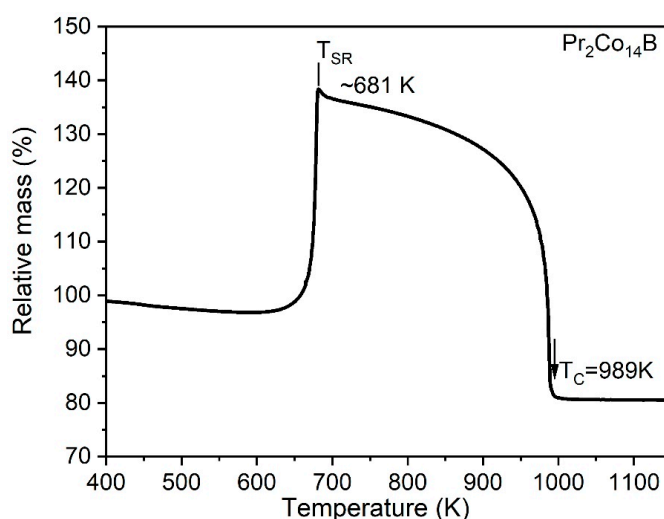


Figure 2. TGA plot for sample annealed at 1270 K for seven days showing Curie temperature at 989 K and spin re-orientation temperature of 681 K.

Figure 3a,b show the XRD results of the as-spun ribbons of the PrCoB-TiC and PrCoB samples, respectively. As already seen from the thermal analyses data, the XRD pattern confirms that the fraction of the amorphous content is higher in the PrCoB-TiC, compared to PrCoB. The significantly higher amorphous content in the PrCoB-TiC indicates the microstructural refinement effect of TiC in $\text{Pr}_2\text{Co}_{14}\text{B}$, similar to reports on Nd-Fe-B based alloys [23,24].

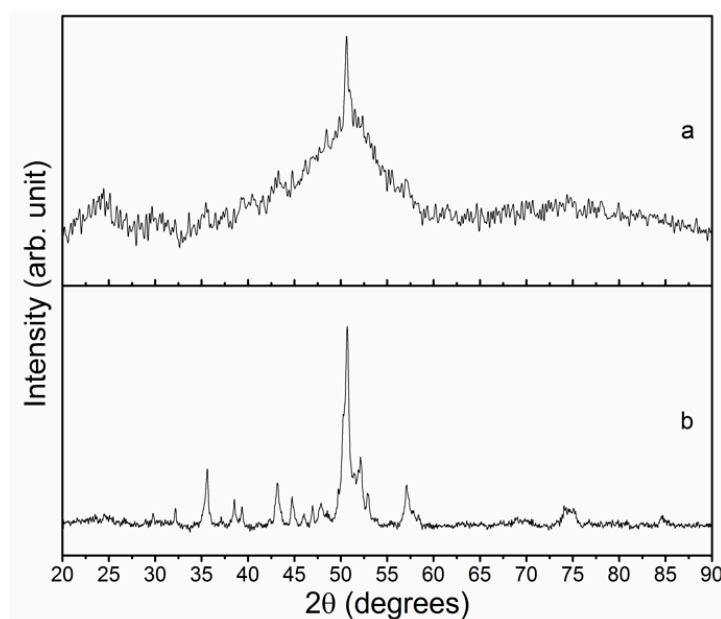


Figure 3. X-ray diffraction pattern of $\text{Pr}_2\text{Co}_{14}\text{B}$ as-spun ribbons with TiC (a) and without TiC (b).

The transmission electron micrographs of the as-spun samples are shown in Figure 4. Micrographs Figure 4a–c correspond to the microstructure of the as-spun PrCoB-TiC samples from wheel side to free side, while Figure 4d–f correspond to the as-spun PrCoB samples, also from wheel side to free side. The diffuse diffraction rings in the as-spun PrCoB-TiC samples indicate that they are predominantly amorphous. This agrees with the absence of a crystallization peak in Figure 1a and the XRD pattern in Figure 3a. The bright contrasts in the PrCoB-TiC samples are Ti-rich phase (TiC). In contrast, the as-spun PrCoB samples show obvious signs of crystallinity with grain size in the range of 20–200 nm, from wheel side to free side. The crystalline nature of PrCoB agrees with the observation of crystallization peak in Figure 1b and the sharp X-ray diffraction patterns in Figure 3b. The grain sizes are also non-uniform from the wheel to the free side of the melt-spun ribbons. These results show the ability to refine the microstructure of Pr-Co-B systems with TiC. The microstructural refinement is related to the reduced growth rate of the solidification front in the samples with TiC which provides the ability to control the microstructure and optimize magnetic properties. Similar effect has been previously reported for Nd-Fe-B systems [27,28]. In the Nd-Fe-B systems, it was shown that over quenched conditions can be achieved at slower wheel speeds with TiC addition but at higher wheel speeds without TiC [24].

In Figure 5, micrographs Figure 5a–c correspond to the microstructure of the heat treated PrCoB-TiC samples from wheel side to free side, while Figure 5d–f correspond to the heat treated PrCoB samples, also from wheel side to free side. It can be seen that TiC enables greater control of the microstructural development in large volume fraction of $\text{Pr}_2\text{Co}_{14}\text{B}$ ribbons during heat treatment. PrCoB-TiC samples (Figure 5a–c) show relatively uniform grain sizes from wheel to free sides of the ribbon, with an average grain size of 100 nm. Under the same heat treatment conditions, the morphology of the grains in PrCoB samples (Figure 5d–f) changes significantly from the wheel to free side. Closer to wheel side, fine grain sizes (~25 nm) with high density of stacking faults were observed. On the free side of the ribbon however, the PrCoB samples show an average grain size of 200 nm with almost no stacking faults, compared with the wheel side of the ribbons. The TiC particles in PrCoB-TiC can be seen as bright contrasts in Figure 5a–c with grain size of ~20 nm. Most of TiC can be seen near grain boundaries and triple junctions. The effect of TiC on limiting grain growth can be easily seen by comparing Figure 5c,f.

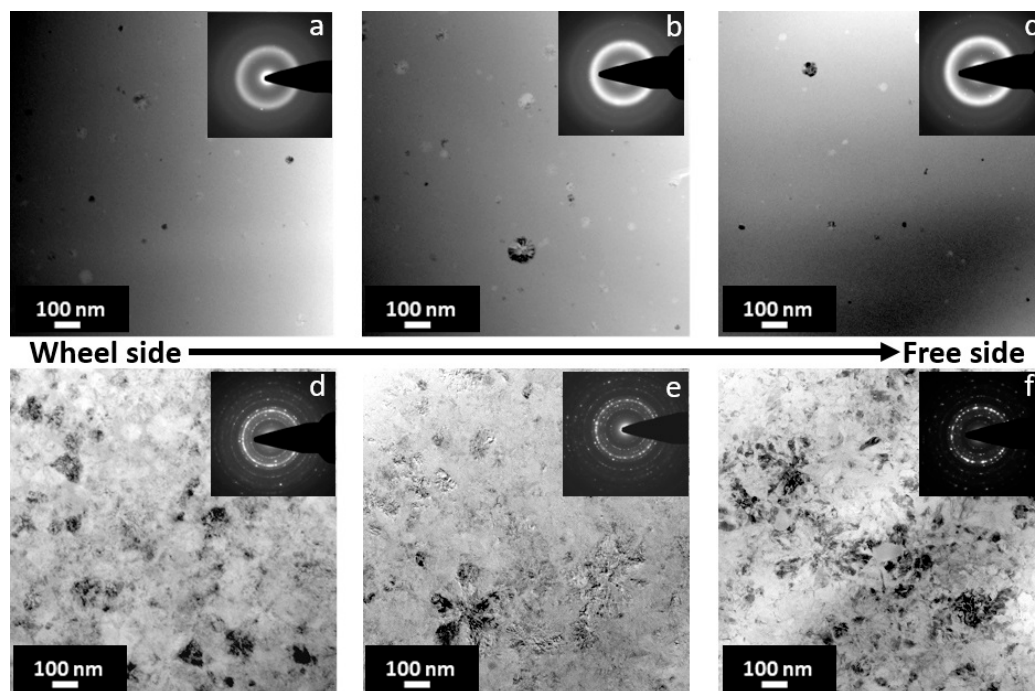


Figure 4. Transmission electron micrographs and corresponding selected area electron diffraction pattern of the as-spun $\text{Pr}_2\text{Co}_{14}\text{B}$ samples performed across the thickness of the ribbons with TiC ((a–c): wheel side to free side) and without TiC ((d–f): wheel side to free side).

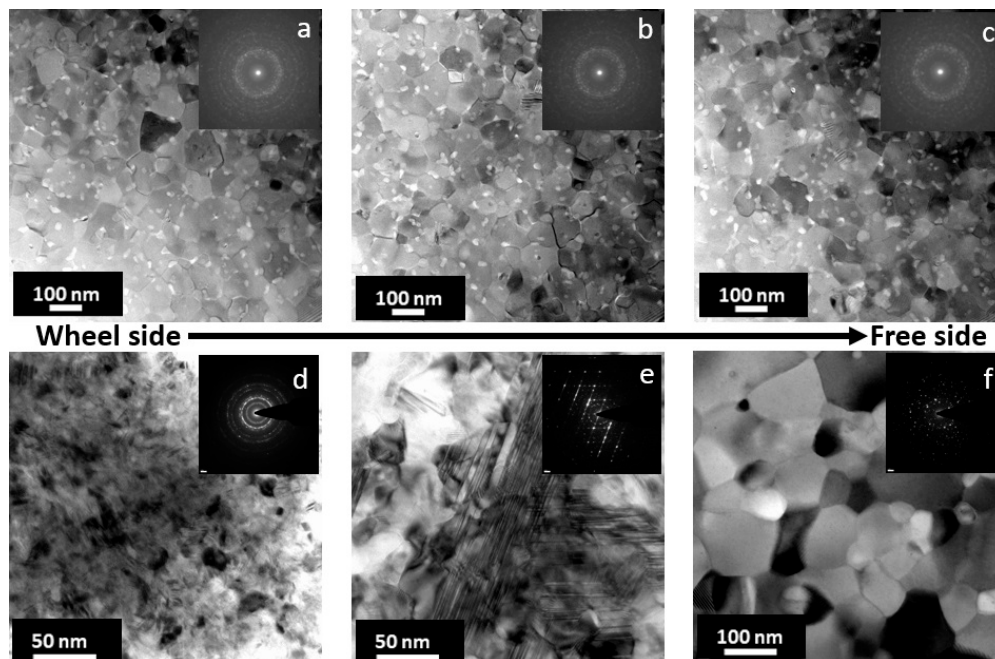


Figure 5. Transmission electron micrographs and corresponding selected area electron diffraction pattern of the heat treated $\text{Pr}_2\text{Co}_{14}\text{B}$ samples performed across the thickness of the ribbons with TiC ((a–c): wheel side to free side) and without TiC ((d–f): wheel side to free side).

The elemental mapping of the PrCoB-TiC in Figure 6 shows that the TiC and $\text{Pr}_2\text{Co}_{14}\text{B}$ co-exist with, at least, two other phases in the microstructure. The phase labelled “rare-earth rich phase” has Pr to Co ratio of 1:1.7 which is closer in composition to PrCo_2 . A phase with composition PrCo_2 was also observed closer to the wheel side in the PrCoB sample. The phase labelled “rare-earth lean phase” is predominantly Co with some Ti at a ratio of 8.4:1. Like in the Nd-Fe-B system [27], there was no Ti or

C found in the matrix phase which indicates that with both elements present, they have significantly low solubility in $\text{Pr}_2\text{Co}_{14}\text{B}$. With only Ti, it was found that TiB_2 formed in addition to Nd-Fe-B [27]. The formation of extra phases in the present study may indicate that less than 3 wt.% of TiC is needed for optimum grain refinement. We intend to investigate the ability to use less refractory carbide in the future because such will be very useful in minimizing the reduction in magnetization due to presence of non-magnetic phases.

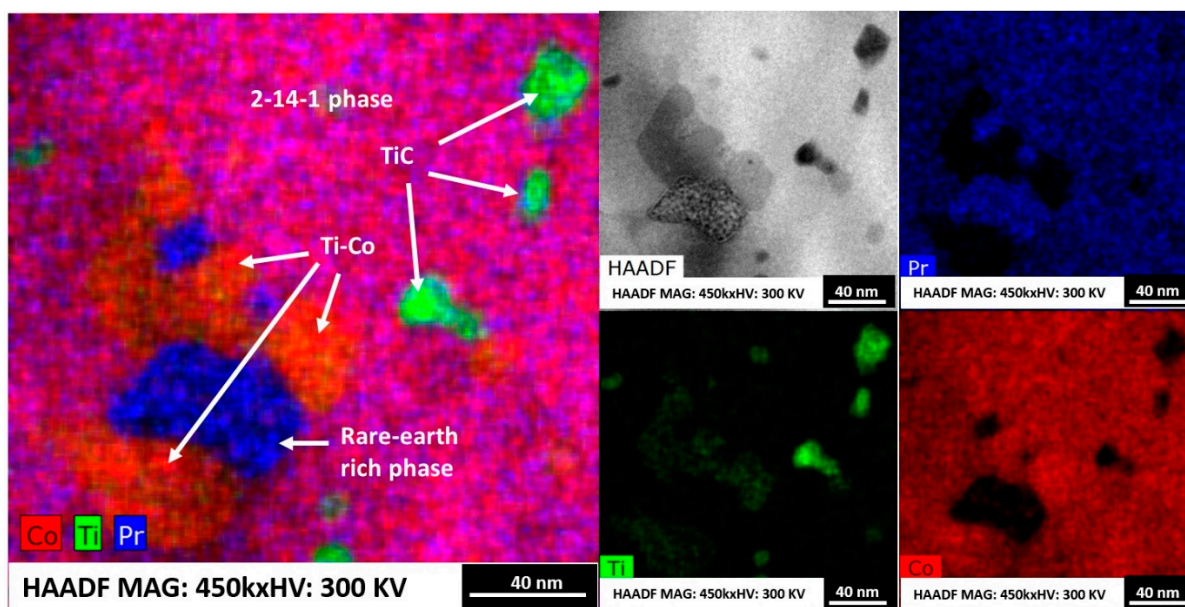


Figure 6. Elemental mapping of the heat treated $\text{Pr}_2\text{Co}_{14}\text{B}$ sample with TiC.

Figure 7 shows the room temperature magnetic hysteresis loops of the as-spun PrCoB-TiC and PrCoB samples. Typical of amorphous hard magnetic materials, the as-spun PrCoB-TiC sample showed a hysteresis loop corresponding to soft magnetic materials. This agrees with the observed microstructure and crystal structure of the sample. The as-spun PrCoB shows a hysteresis loop typical of hard magnetic materials containing significantly more crystalline than amorphous fraction, which also corresponds to previously discussed results. The observation that PrCoB-TiC approaches saturation faster than PrCoB is also indicative of higher amount of crystalline hard magnetic materials in the as-spun PrCoB . The higher magnetization at 30 kOe obtained for the as-spun PrCoB , compared to the as-spun PrCoB-TiC is likely due to the dilution of the magnetization of the $\text{Pr}_2\text{Co}_{14}\text{B}$ by non-magnetic TiC phase.

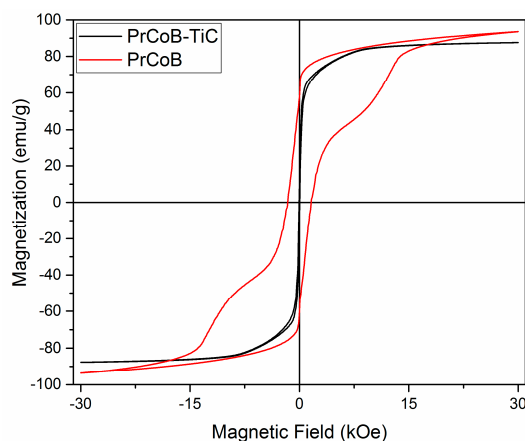


Figure 7. Hysteresis loop of as-spun $\text{Pr}_2\text{Co}_{14}\text{B}$ with and without TiC.

The magnetic hysteresis loops of the samples annealed at 1020 K (above the crystallization temperature) for 15 min were measured up to 90 kOe and are shown in Figure 8. Hard magnetic properties developed upon annealing resulting in higher coercivity materials, compared to the as-spun samples. Nearly twice the coercivity of the annealed PrCoB was obtained for the annealed PrCoB-TiC samples. Since heat treatment is necessary to fully develop the hard magnetic microstructure, the grain refining effect of TiC provides a greater ability to control the microstructure during such heat treatments which leads to enhanced hard magnetic properties. TiC altered the growth kinetics and limited the formation of abnormal grain growth so that more uniform microstructure can be obtained over a volume of the materials. In Nd-Fe-B system, average grain size of ~75 nm and 200 nm were reported for samples with and without TiC, respectively [23,24]. In the present study, the average grain size was ~100 nm for the PrCoB-TiC sample. The finer grains provide greater pinning sites to magnetic domains which leads to the observed increase in coercivity. The difference in magnetization between both samples is greater in the annealed samples, compared to the as-spun. It is thus likely that the phases labelled as “rare-earth-rich phase” and “rare-earth-lean phase” in Figure 6 further reduced magnetization in the sample with TiC.

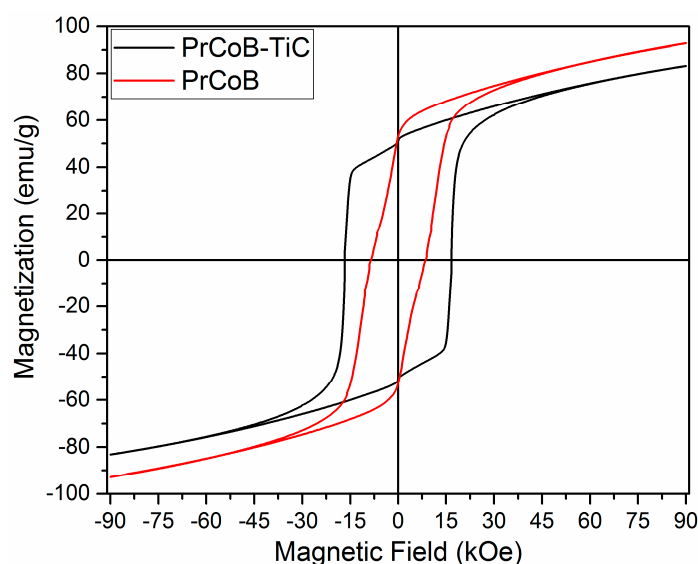


Figure 8. Hysteresis loop of the $\text{Pr}_2\text{Co}_{14}\text{B}$ ribbons annealed at 750 °C for 15 min, with and without TiC.

It can be seen in Figure 8 that the magnetization for both samples did not approach saturation at the maximum applied magnetic field of 90 kOe, indicative of high magnetocrystalline anisotropy in Pr-Co-B systems. An anisotropy field of ~158 kOe was estimated for the samples using the method described in the materials and method section. To verify the anisotropy field values, the first quadrant demagnetization curve of both samples in Figure 8 was applied to an approach used by McCallum [29] based on the Stoner-Wohlfarth model, which resulted in a comparable value of ~160 kOe. The observation that both samples have comparable anisotropy fields can also be seen from the similarity in the slopes of their high magnetic field magnetization plots in Figure 8. The anisotropy field obtained for these samples is higher than previously reported for materials based on Pr-Co-B (97–125 kOe) [21,30]. One may expect that such comparable anisotropy field would correspond to comparable coercivity for both PrCoB and PrCoB-TiC, which was not the case. This indicates that the higher coercivity obtained for the PrCoB-TiC is mainly due to microstructural refinement effect of TiC and highlights the fact that coercivity is an extrinsic magnetic property. The step near remanence in PrCoB-TiC is likely due to the magnetic properties of the predominantly cobalt phase seen in the TEM since the other secondary phase, PrCo_2 , is paramagnetic above ~40 K [31].

Extrapolating the magnetization to saturation using the aforementioned model [30] yields an estimated saturation magnetization of 107 emu/g for PrCoB-TiC and 120 emu/g for PrCoB. This

indicates that under anisotropic conditions, it is possible to develop permanent magnets with maximum energy product of ~30 MGOe with these alloys. It suggests the ability to develop permanent magnets comparable in properties with high performance Sm-Co based magnets. However Pr-Co-B has spin-reorientation at 680 K which is below its Curie temperature of 990 K. At spin reorientation, magnetization switches from easy axis to easy plane which diminishes magnetocrystalline anisotropy and coercivity. Substituting ~36% or more of the Co concentration with Fe results in materials without spin-reorientation with Curie temperature of ~942 K [32]. Such substitution also results in increased magnetization although coercivity is reduced [33]. Addition of TiC can therefore limit the decrease in coercivity due to Fe-substitution in Pr-Co-B whilst resulting in materials without spin-reorientation. If smaller amount of TiC is sufficient for optimum microstructural refinement, magnetization can further be increased by reducing the amount of TiC used; hence improving the potential energy product of the alloys.

4. Conclusions

This study shows that the microstructure of melt-spun $\text{Pr}_2\text{Co}_{14}\text{B}$ is greatly refined by the addition of TiC. No obvious changes in the magnetic anisotropy field was observed, indicating that the observed significant increase in coercivity (nearly twice) is due to microstructural optimization effects of the TiC. Magnetization decreased due to the addition of non-magnetic TiC and the formation of low magnetic moment secondary PrCo_2 and Co-rich phases. However, the remanence is comparable for samples with and without TiC. Also, neither Ti nor C were found in the 2:14-1 phase. Formation of secondary phase was discussed as an indication of the opportunity to reduce the TiC content whilst achieving significant increase in coercivity and comparable values of remanence and saturation magnetization.

Author Contributions: Conceptualization, I.C.N. and R.W.M.; Funding acquisition, R.W.M.; Investigation, I.C.N., M.H., K.S., L.Z., R.W.M. and M.J.K.; Methodology, I.C.N. and M.H.; Resources, M.J.K.; Supervision, R.W.M. and M.J.K.; Writing—original draft, I.C.N. and M.H.; Writing—review & editing, I.C.N., L.Z. and M.J.K.

Funding: This research was supported by the Critical Materials Institute, an Energy Innovation Hub funded by the U.S. Department of Energy, Office of Energy Efficiency and Renewable Energy, Advanced Manufacturing Office.

Conflicts of Interest: The authors declare no conflict of interest.

References

1. Herbst, J. $\text{R}_2\text{Fe}_{14}\text{B}$ materials: Intrinsic properties and technological aspects. *Rev. Mod. Phys.* **1991**, *63*, 819–898. [[CrossRef](#)]
2. Sagawa, M.; Fujimura, S.; Yamamoto, H.; Matsuura, Y.; Hiraga, K. Permanent magnet materials based on the rare earth-iron-boron tetragonal compounds. *IEEE Trans. Magn.* **1984**, *20*, 1584–1589. [[CrossRef](#)]
3. Seo, Y.; Morimoto, S. Comparison of dysprosium security strategies in Japan for 2010–2030. *Resour. Policy* **2014**, *39*, 15–20. [[CrossRef](#)]
4. Bai, G.; Gao, R.W.; Sun, Y.; Han, G.B.; Wang, B. Study of high-coercivity sintered NdFeB magnets. *J. Magn. Mater.* **2007**, *308*, 20–23. [[CrossRef](#)]
5. Herrault, F.; Arnold, D.P.; Zana, I.; Galle, P.; Allen, M.G. High temperature operation of multi-watt, axial-flux, permanent-magnet microgenerators. *Sens. Actuators A Phys.* **2008**, *148*, 299–305. [[CrossRef](#)]
6. Sasaki, T.T.; Ohkubo, T.; Hono, K. Structure and chemical compositions of the grain boundary phase in Nd-Fe-B sintered magnets. *Acta Mater.* **2016**, *115*, 269–277. [[CrossRef](#)]
7. Nakamura, T.; Yasui, A.; Kotani, Y.; Fukagawa, T.; Nishiuchi, T.; Iwai, H.; Akiya, T.; Ohkubo, T.; Gohda, Y.; Hono, K.; et al. Direct observation of ferromagnetism in grain boundary phase of Nd-Fe-B sintered magnet using soft x-ray magnetic circular dichroism. *Appl. Phys. Lett.* **2014**, *105*, 202404. [[CrossRef](#)]
8. Zhou, Q.; Liu, Z.W.; Zhong, X.C.; Zhang, G.Q. Properties improvement and structural optimization of sintered NdFeB magnets by non-rare earth compound grain boundary diffusion. *Mater. Des.* **2015**, *86*, 114–120. [[CrossRef](#)]

9. Bae, K.-H.; Kim, T.-H.; Lee, S.-R.; Kim, H.-J.; Lee, M.-W.; Jang, T.-S. Magnetic and microstructural characteristics of DyF₃/DyH_x dip-coated Nd–Fe–B sintered magnets. *J. Alloys Compd.* **2014**, *612*, 183–188. [[CrossRef](#)]
10. Gabay, A.M.; Hu, X.C.; Hadjipanayis, G.C. Mechanochemical synthesis of fine R₂Fe₁₄BH_x and R₂Fe₁₄B powders with R=Nd or Nd–Dy. *J. Alloys Compd.* **2013**, *574*, 472–476. [[CrossRef](#)]
11. Ucar, H.; Parker, D.S.; Nlebedim, I.C.; McCallum, R.W.; McCall, S.K.; Paranthaman, M.P. Strategic coating of NdFeB magnets with Dy to improve the coercivity of permanent magnets. *Adv. Mater. Res.* **2015**, *4*, 227–233. [[CrossRef](#)]
12. Liang, L.; Ma, T.; Zhang, P.; Jin, J.; Yan, M. Coercivity enhancement of NdFeB sintered magnets by low melting point Dy_{32.5}Fe₆₂Cu_{5.5} alloy modification. *J. Magn. Magn. Mater.* **2014**, *355*, 131–135. [[CrossRef](#)]
13. Rodewald, W.; Katter, M. Properties and Applications of High Performance Magnets. VACUUMSCHMELZE GmbH Co. KG. (n.d.) Available online: https://www.vacuumschmelze.de/fileadmin/documents/pdf/fipublikationen/Paper_HPMA_2004_Magnets.pdf (accessed on 12 November 2018).
14. EEC. Neodymium Iron Boron Magnets. Electron Energy Corp. (n.d.) Available online: <http://www.electronenergy.com/neodymium-iron-boron-magnets/> (accessed on 12 November 2018).
15. Manthey, N. Samsung SDI to Reduce Cobalt in Its Batteries to Zero. Electrive.Com. 2018. Available online: <https://www.electrive.com/2018/02/12/samsung-sdi-reduce-cobalt-batteries-zero/> (accessed on 12 November 2018).
16. Bailey, M.P. Cabot to Develop Low-Cobalt Cathodes for DOE's Lithium-Ion Battery Research Project. Chemical Engineering. 2018. Available online: <https://www.chemengonline.com/cabot-to-develop-low-cobalt-cathodes-for-does-lithium-ion-battery-research-project/?printmode=1> (accessed on 12 November 2018).
17. Christodoulou, C.N.; Massalski, T.B.; Wallace, W.E. Magnetic hardening of the Pr₂Co₁₄B-based rapidly quenched alloys. *J. Magn. Magn. Mater.* **1993**, *125*, 177–189. [[CrossRef](#)]
18. Pan, S. *Rare Earth Permanent Magnet Alloys' High Temperature Phase Transformation: In Situ and Dynamic Observation and Its Application in Material Design*; Springer: New York, NY, USA, 2013.
19. Christodoulou, C.N.; Wallace, W.E.; Massalski, T.B. Magnetic hardening of Pr-Co-B sintered magnets (abstract). *J. Appl. Phys.* **1990**, *66*, 2749–2751. [[CrossRef](#)]
20. Buschow, K.H.J.; de Mooij, D.B.; Sinnema, S.; Radwanski, R.J.; Franse, J.J.M. Magnetic and crystallographic properties of ternary rare earth compounds of the type R₂Co₁₄B. *J. Magn. Magn. Mater.* **1985**, *51*, 211–217. [[CrossRef](#)]
21. Shimao, M.; Ido, H.; Kido, G.; Ohashi, K. Magnetic properties of R₂Co₁₄B (R = rare earth). *IEEE Trans. Magn.* **1987**, *23*, 2722–2724. [[CrossRef](#)]
22. Fuerst, C.D.; Herbst, J.F.; Pinkerton, F.E. Magnetic hardening of Pr₂Co₁₄B. *J. Appl. Phys.* **1988**, *64*, 5556–5558. [[CrossRef](#)]
23. Tang, W.; Wu, Y.Q.; Dennis, K.W.; Kramer, M.J.; Anderson, I.E.; McCallum, R.W. Effect of TiC addition on microstructure and magnetic properties for MRE₂(Fe,Co)₁₄B melt-spun ribbons (MRE=Nd+Y+Dy). *J. Appl. Phys.* **2006**, *99*, 08B510. [[CrossRef](#)]
24. Kramer, M.J.; Li, C.P.; Dennis, K.W.; McCallum, R.W.; Sellers, C.H.; Branagan, D.J.; Lewis, L.H.; Wang, J.Y. Effect of TiC additions to the microstructure and magnetic properties of Nd_{9.5}Fe_{84.5}B₆ melt-spun ribbons. *J. Appl. Phys.* **1998**, *83*, 6631–6633. [[CrossRef](#)]
25. Ucar, H.; Nlebedim, I.C.; Paranthaman, M.P.; McCallum, R.W. Evolution of structural and magnetic properties due to nanocrystallization of mechanically milled amorphous Pr-Co-B powders. *J. Appl. Phys.* **2014**, *116*, 233901. [[CrossRef](#)]
26. Pedziwiatr, A.T.; Wallace, W.E. Spin arrangements in R₂Co₁₄B compounds (R = rare earth). *Solid State Commun.* **1986**, *60*, 653–655. [[CrossRef](#)]
27. Branagan, D.J.; McCallum, R.W. Precipitation phenomenon in stoichiometric Nd₂Fe₁₄B alloys modified with titanium and titanium with carbon. *J. Alloys Compd.* **1995**, *230*, 67–75. [[CrossRef](#)]
28. Merkulova, G.Y.; Margulies, L.; Dennis, K.W.; McCallum, R.W. The temperature dependence of coercivity in nanocrystalline Nd–Fe–B–(TiC) magnets. *J. Appl. Phys.* **2000**, *87*, 4738–4740. [[CrossRef](#)]
29. McCallum, R.W. Determination of the saturation magnetization, anisotropy field, mean field interaction, and switching field distribution for nanocrystalline hard magnets. *J. Magn. Magn. Mater.* **2005**, *292*, 135–142. [[CrossRef](#)]

30. Chuang, Y.C.; Wu, C.H.; Chang, T.D.; Wang, F.H.; De Boer, F.R. Structure and magnetic properties of cobalt-rich Pr-Co-B alloys. *J. Less Common Met.* **1988**, *144*, 249–255. [[CrossRef](#)]
31. de Jongh, L.J.; Bartolomé, J.; Greidanus, F.J.A.M.; de Groot, H.J.M.; Stipdonk, H.L.; Buschow, K.H.J. Magnetic properties of PrCo₂ and its ternary hydride PrCo₂H₄. *J. Magn. Magn. Mater.* **1981**, *25*, 207–214. [[CrossRef](#)]
32. Pedziwiatr, A.T.; Wallace, W.E. Spin reorientations in R₂Fe_{14-x}Co_xB systems (R = Pr, Nd and Er). *J. Magn. Magn. Mater.* **1987**, *65*, 139–144. [[CrossRef](#)]
33. Chen, R.; Guo, S.; Wang, J.; Lee, D.; Yan, A. The microstructure and magnetization behaviors of (Pr_{8,2}Fe_{86.12x}Co_xB_{5.7})_{0.99}Zr_{0.01} (x = 0–10) nanocomposite magnets. *J. Appl. Phys.* **2011**, *109*, 07A756. [[CrossRef](#)]



© 2019 by the authors. Licensee MDPI, Basel, Switzerland. This article is an open access article distributed under the terms and conditions of the Creative Commons Attribution (CC BY) license (<http://creativecommons.org/licenses/by/4.0/>).